Effect of building directions on the surface roughness, microstructure, and tribological properties of selective laser melted Inconel 625

Xingchen Yan, Shuohong Gao, Cheng Chang, Jian Huang, Khashayar Khanlari, Dongdong Dong, Wenyou Ma, Nouredine Fenineche, Hanlin Liao, Min Liu

Effect of building directions on the surface roughness, microstructure, and tribological properties of selective laser melted Inconel 625

Xingchen Yan [1, 2, a], Shuohong Gao [2, a], Cheng Chang [3, *], Jian HUANG [1, *], Khashayar Khanlari [4], Dongdong Dong [1], Wenyou Ma [1], Nouredine Fenineche [2], Hanlin Liao [2], Min Liu [1]

1. *Guangdong Academy of Sciences, Guangdong Institute of New Materials, National Engineering Laboratory for Modern Materials Surface Engineering Technology, The Key Lab of Guangdong for Modern Surface Engineering Technology, Guangzhou 510650, P.R. China*
2. *ICB UMR 6303, CNRS, Univ. Bourgogne Franche-Comté, UTBM, F-90010 Belfort, France*
3. *ICD-LASMIS, UMR CNRS 6281, University of Technology of Troyes, 12 rue Marie Curie, CS 42060, 10004, Troyes Cedex, France*
4. *Guangdong Institute of Materials and Processing, Guangzhou 510650, P.R. China*

Abstract

To study the effect of the building directions on surface macro- / micro- structure and tribological properties of Inconel 625 samples manufactured by selective laser melting (SLM) technology, parts were fabricated in three different building directions (0°, 45°, 90°). The microstructure of SLM samples was characterized using optical microscope (OM) and scanning electron microscopy (SEM). Only the γ-Ni phase was detected in the X-ray diffraction (XRD) patterns of the SLM samples. The lattice constant of the γ-Ni phase in the SLM 45°sample was the lowest among these SLM samples. The value of the surface roughness of the SLM 45° specimen was the highest than other parts, while, the value of the surface roughness of the SLM 0° sample was the lowest. The surface microstructure of the SLM samples was primarily composed of columnar dendrites and equiaxed grains. Among these samples, the finest equiaxed grains (about 0.38-0.63 μm) was evenly distributed in the SLM 0° sample, while, the roughest equiaxed grains (approximately 0.73-1.26 μm) was formed in the SLM 45° sample. Furthermore, the SLM 0° specimen showed the highest microhardness value (332 $HV_{0.2}$) and the best tribological performances, such as the lowest average coefficient of friction (COF=0.31) and the wear rate (57.2×10^{-6} mm^3 / (N•m)).

[a] These two authors contributed equally to this work.
*Corresponding authors.
Cheng CHANG: cheng.chang1993@hotmail.com.
Jian HUANG: huangjian@gdinm.com.

Keywords: Selective laser melting, building directions, Surface roughness, Microstructure evolution, Tribological performances.

1 Introduction

When it comes to the metal additive manufacturing (AM) technology, selective laser melting (SLM), the represent of sustainable metal production, is one of the most attracting technologies employed in recent years, as stated by Chen et al. (2019) and Martin et al. (2017). In the process of the SLM, metal powder is spread in thin layers and rapidly fused using high-density laser beam in the layer-by-layer method in order to create object components with complex geometric shapes. This technique opens a wide field of possible applications for many industrial sectors thanks to its eye-catching advantages, such as unlimited geometric variability, design freedom and material flexibility, as revealed by Yan et al. (2019b) and Yan et al. (2019a). Also, apart from the commonly used commercial pre-alloyed powder e.g., nickel-based, cobalt-based, and iron-based alloy powder, this technique, due to the high energy density of the input laser beam, can also manufacture high melting point refractory metals like molybdenum, tantalum, tungsten and their alloys. SLM technology can, therefore, be regarded as an emerging technology to produce metal components directly from the raw material.

Inconel 625 is a nickel-based superalloy promoted by solid-solution hardening of various elements like C, Cr, Mo, and Nb, which has been used in widespread applications such as aerospace, marine, chemical and nuclear industries due to its outstanding yield, tensile and creep strength at elevated temperature, as investigated by Paul et al. (2007). Inconel 625 components are generally manufactured by conventional manufacturing processes e.g., casting, powder metallurgy and stir friction welding (Song and Nakata, 2010). With the bombarding development of AM technology, manufacturing Inconel 625 components by AM for industrial applications has steadily emerged as a promising approach. Currently, in the review paper by Mumtaz and Hopkinson (2009), the SLM technology was reported to successfully fabricate Inconel 625 parts. Compared to other AM techniques such as direct metal deposition (DMD) technology (Dinda et al., 2009), SLM, being able to efficiently utilize material and achieve cost-effective processing, has obtained a great attention. The investigations conducted by Frazier (2014), Yadollahi and Shamsaei (2017) and Yap et al. (2015) showed that since the laser spot of SLM is focused in a tiny area of less than 100 μm in diameter, extremely high temperature is generated in the center of the laser molten pool. Also, owing to energy distribution occurring in the laser spot, a great thermal gradient in the Inconel 625 material is produced, which directly affects the microstructure and mechanical performances of the processed parts.

To research the microstructure characteristics of the SLM Inconel 625 parts, recently, some studies focusing on the microstructure features of this material have been published. Li

et al. (2017) found that fine columnar γ dendrite microstructure with strong texture was a significant feature of the SLM samples, and the heat treatment could recrystallize microstructures, increase grain size, decrease dislocation density and diminish grain boundary misorientation. Anam et al. (2014) investigated that cellular substructure grains with enriched zones of Nb and Mo in the inter-arm spacing were detected using SEM and EDS, and the grains were also proved to grow preferentially in the build direction within the microstructure of SLM Inconel 625 parts. Li et al. (2015) studied the microstructure evolution of SLM Inconel 625 components and concluded that the microstructure was composed of elongated columnar crystals. In addition, they reported that the effect of the applied heat treatment on the microstructures of the SLM parts was not significant. Though many scholars have done various experiments for describing the microstructure features of SLM Inconel 625 parts in the different heat-treated states, the effect of the building directions on the microstructure of the surface and its evolution are still rarely analyzed.

As well known, manufacturing methods have a great impact on the microstructure and mechanical performances of the SLM Inconel 625 parts. Therefore, some other researchers have also studied the impact of applying different SLM manufacturing strategies on the microstructure and mechanical properties of the SLM Inconel 625 parts. Yadroitsev et al. (2009) investigated the effect of the different building directions on the mechanical properties of the SLM Inconel 625 parts, and the results displayed that the Young's modulus value for the "horizontal" samples was by 1.5 times higher than that for the "vertical" specimens and was close to that of wrought Inconel 625 component (about 200 GPa). However, the yield strength and ultimate strength of the samples were not significantly affected by the change in the building directions. Yadroitsev and Smurov (2010) also found that elongation of the SLM Inconel 625 parts was only 8-10 % compared to 40 % for conventionally cast and wrought components. Moreover, Gonzalez et al. (2019) compared the microstructures and mechanical properties of Inconel 625 parts produced by different AM techniques. The results illustrated that SLM specimens had potential to display outstanding mechanical properties as compared to ones fabricated using other technologies. As described above, the majority of the current studies were primarily concentrated on the effect of laser processing parameters and building directions on the microstructure and mechanical properties of SLM parts.

In summary, building directions can be adjusted to modify the microstructure of the SLM components, as demonstrated by Rashid et al. (2018). However, to date, the impact of the building directions upon the surface microstructure of the SLM Inconel 625 components, particularly the diverse microstructure caused by the complex thermal history and micro-reaction occurring in the SLM process, has not been explored in depth. Besides, relationships existing between the printing orientations and the tribological behavior of the SLM Inconel 625 parts have not been systematically studied, either. Obviously, there is still a research gap about the effect of SLM building directions on the wear performance of the SLM Inconel 625 samples.

Hence, this problem should be of great interest to researchers as it not only helps to dig in the depth of the wear mechanism of SLM parts but also is deemed to be useful for the design and fabricating strategy of SLM components for generating high wear-resistant surfaces. Thus, the influence of the building directions on the macrostructure characteristics such as surface roughness, the surface microstructure evolution, and the wear mechanism of the SLM Inconel 625 parts are discussed and analyzed in detail within this work.

2 Experimental details

2.1. Manufacturing procedure

In this work, Inconel 625 powder (EOS GmbH, Germany) with a spherical shape was used as the raw material. The chemical composition of this used powder is shown in Table 1. The overview and magnified surface morphology of the used Inconel 625 powder are displayed in Fig. 1a. The particle size distribution (d_{10}=23.3 μm, d_{50}=34.3 μm, and d_{90}=49.6 μm) of the powder, measured by the laser diffraction powder sizer (Mastersizer 2000, Malvern Instruments Ltd., UK), is given in Fig. 1b. As described in Fig. 1c, the laser scanning strategy was chosen as zigzag pattern with 67° rotation between the neighboring layers. These specimens were built up in three different orientations by SLM using an EOS M290 (EOS GmbH, Germany) system. As shown in Fig. 1d, the different category of the processed samples is marked as 0°, 45°, 90°. After conducting a systematic investigation, laser spot of 100 μm, laser power of 280 W, layer thickness of 30 μm, hatch distance of 110 μm and scanning speed of 950 mm/s were used to process these samples. In order to avoid oxidation, the chamber of the SLM machine was filled with high purity nitrogen (99.99 %) to maintain the residual oxygen content below 0.13 %.

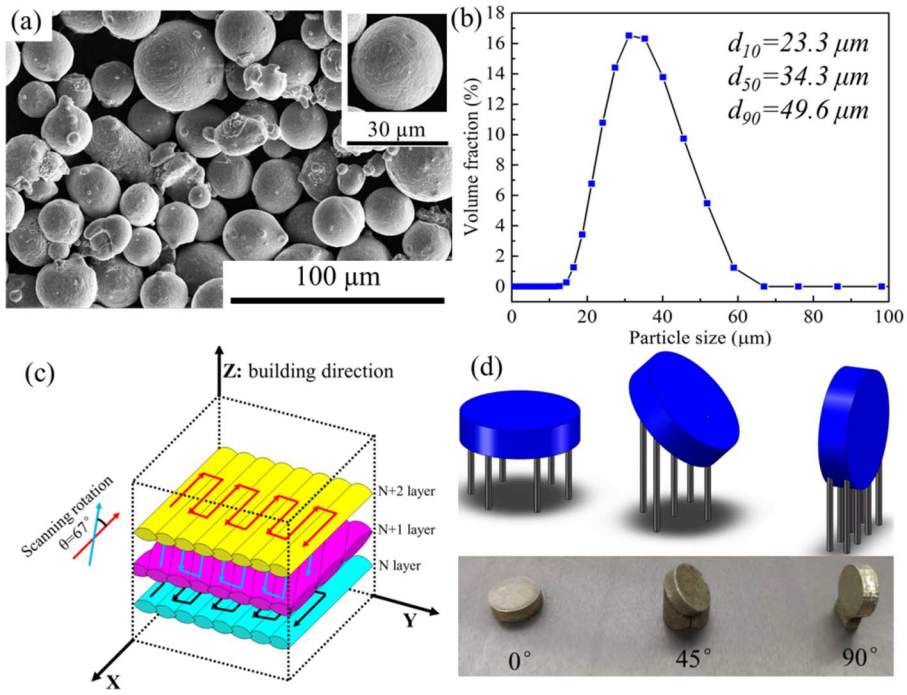

Figure 1. (a) Macroscopic morphology of the raw material; (b) particle size distribution; (c) SLM scanning strategy used to process the samples; (d) SLM Inconel 625 samples produced by applying different building directions.

Table 1: Chemical composition of the Inconel 625 raw powder

Element	Ni	Cr	Mo	Nb	Fe	Co	Al	C
wt.%	Balance	20.00-23.00	8.40-10.00	3.15-4.15	≤5.00	≤1.00	≤0.40	≤0.10

2.2. Material characterization

The surface roughnesses of these SLM parts were evaluated by a DektakXT profilometer (Bruker, American). The surface area of 1000 μm×1000 μm of the each SLM sample at different building directions was selected as the surface roughness test plane. The surface microstructure characteristics of the SLM Inconel 625 samples were observed using an optical microscope (OM, Leica Dmi5000m) and a scanning electron microscopy (FEI Nova Nano SEM 450). Before conducting the metallographic analyses, all the samples were polished by SiC grinding papers with different grits and then etched for 20 s in aqua regia solution containing 100 ml HNO_3 and 300 ml HCl. Phase composition of the SLM parts was utilized by X-ray diffraction (XRD, Siemens, Germany) at 40 kV and 40 mA in a 2θ range of 30-100°.

2.3. Mechanical performances

The Vickers microhardness was measured using a microhardness tester (Leitz-Wetzlar, Germany) with a load of 200 g and an indentation time of 25 s. Before testing the

microhardness, surface roughness of the testing plane of the each SLM sample were polished to below 0.15 μm. The microhardness values were recorded after measuring different locations on each surface of the SLM specimens, and then the average value of 10 times measurements was calculated.

Dry sliding ball-on-disk wear tests were evaluated at room temperature with a CSEM tribometer equipment. Before testing the friction and wear performance, the surface roughness (Ra) of all SLM specimens were polished to below 0.15 μm. Si_3N_4 balls with a 4 mm diameter, cleaned with ethanol before performing the tests, were chosen as the counterpart material sliding on the produced samples. The wear test conditions included a testing load of 500 g, a rotational speed of 100 mm/s, a sliding distance of 200 m, and a rotation radius of 3 mm. The coefficient of friction (COF) was automatically recorded by the machine during the sliding tests. The worn surface of each sample was observed and analyzed by SEM after finishing the wear tests. The macroscopic morphology of the worn tracks was measured by the 3D surface profilometer. The wear rate (ω) of the samples was calculated via the formula as follows and counted the mean value after three measurements:

$$\omega = \frac{2\pi r S}{W \times L}$$

where r is the radius of the wear track, mm; S is the cross-sectional area of the worn tracks, mm^2; W is the testing load, N; and L is the sliding distance, m.

3 Results and discussion

3.1 X-ray diffraction analysis

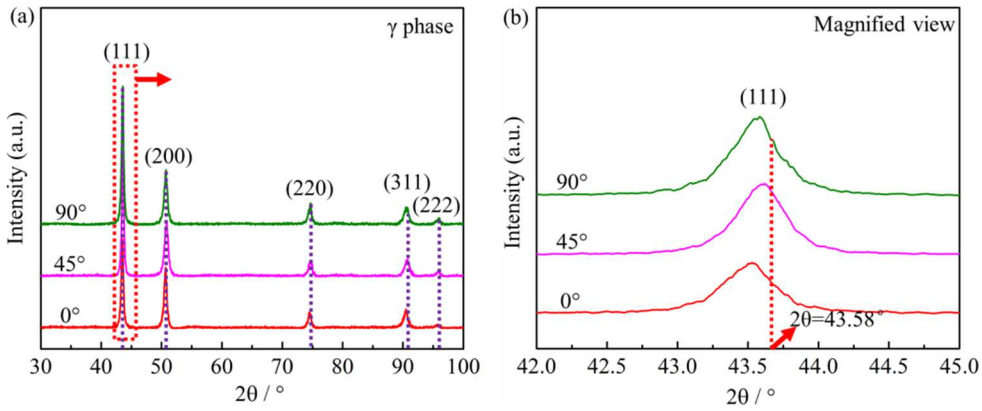

Figure 2. (a) XRD diffractograms of the SLM specimens fabricated in different building directions; (b) the magnified view of the (111) crystal plane

According to the X-ray diffraction patterns of the SLM samples printed in different building directions, as shown in Fig. 2a, only peaks related to γ-Ni (fcc) phase was found. From the phase diagram of the Fe-Cr-Ni ternary alloy, it can be further concluded that the matrix is γ phase with the rather high solubility of Fe in γ-(Cr, Ni) based on the study of Yen

et al. (2008).

The diffraction peaks of some intermetallic phases like γ" phase (Ni_3Nb), Ni_2(Cr, Mo), Laves phase ($NbCr_2$), etc., were not detected, although these intermetallic compounds may have been formed at elevated temperature. The reasons of that may be explained below: as the laser scanning speed (950 mm/s) and the cooling rate of the molten pool (10^5K/s-10^6 K/s (Yan et al., 2020b, 2020a)) were extremely high, these features would cause the velocity of the atomic reconstruction at the front of the solid-liquid interface is quite higher than the diffusion velocity. Hence, the solution atoms were trapped in the solid-liquid interface leading to the occurrence of the so called "solution trapping" phenomenon. Because of this, metallic solute atoms such as Cr, Nb, Mo, and etc., which were enriched at the front of the solid-liquid interface, did not have much chance to form intermetallic compounds and these solute atoms, therefore, were captured in the γ-Ni matrix. As a result, other phases were hard to observe in the XRD patterns of the SLM parts printed in various building directions. Note that a small number of intermetallic compounds might have been formed in the SLM parts, however, probably because of the low content and the small sizes of these precipitates, they were still not presented in the XRD diffractograms (Dinda et al., 2009).

Table 2: Lattice constants of the γ-Ni phase formed in the SLM Inconel 625 parts.

Sample	Lattice constant (Å)	Fitting error
Standard γ-Ni phase measured by Graulis et al. (2009)	3.5911	/
SLM 0° part	3.59474	≤10.33
SLM 45° part	3.59204	≤10.07
SLM 90° part	3.59353	≤10.11

The lattice constants of SLM Inconel 625 parts fabricated in the various building directions were calculated using the Rietveld Refinement method proposed by Alexander and Klue (1989) and Materials Information Company (1991) and are listed in Table 2.

As shown in Fig. 2b, the diffraction peaks of the SLM samples were shifted to a low-angle direction as compared to the (111) crystal plane of the standard γ-Ni phase. Amongst all the printed samples, the offset value of the SLM 45° sample was the lowest. According to Table 2, the measured lattice constants of γ-Ni phase in the SLM parts were larger than the standard lattice constant of γ-Ni phase (a=3.5911 Å), which further led to the occurrence of lattice distortion of the γ-Ni phase. Additionally, the lattice constant measured in the SLM 0° sample was larger than that of the SLM 45° and SLM 90° sample, while, the lattice constant was the lowest in the SLM 45° sample.

Numerous factors such as element solid solution, surface stress, and etc. will lead to the diffraction peak shift and the lattice distortion. As the laser scanning strategy was the same for fabricating these SLM samples, it is estimated that the surface stress was not significantly

different among these SLM specimens. Thus, the difference of the above phenomenon that occurred in the SLM parts could be primarily attributed to the difference existing in the amount of the multi-element solid-solution γ-Ni phase of the printed parts. This situation might be explained by the fact that the solid solubility of the alloying elements was high within the fine microstructure of the SLM 0° sample due to the extremely rapid solidification rate. In contrast, as the cooling rate might be relatively slower during the solidification process of the SLM 45° and the SLM 90° samples, there might have been enough time for the diffusion process of the alloying elements in these samples. As such, it is thought that a supersaturated solid-solution γ-Ni phase with slightly lower solid solubility was produced in the mentioned samples as compared to that of the SLM 0° sample.

After considering the above results and researching the analysis of Aliofkhazraei (2015) and Cieslak et al. (1988), the formation sequence of the phases after solidification of the molten pool can be proposed as follows:

$$\mathrm{L} \rightarrow \mathrm{L} + \gamma - (\mathrm{Cr}, \mathrm{Ni}) \rightarrow \gamma - (\mathrm{Cr}, \mathrm{Ni}) + \text{intermetallic phases}$$

3.2 Macro- / Micro-structure characteristics

3.3.1 Surface roughness

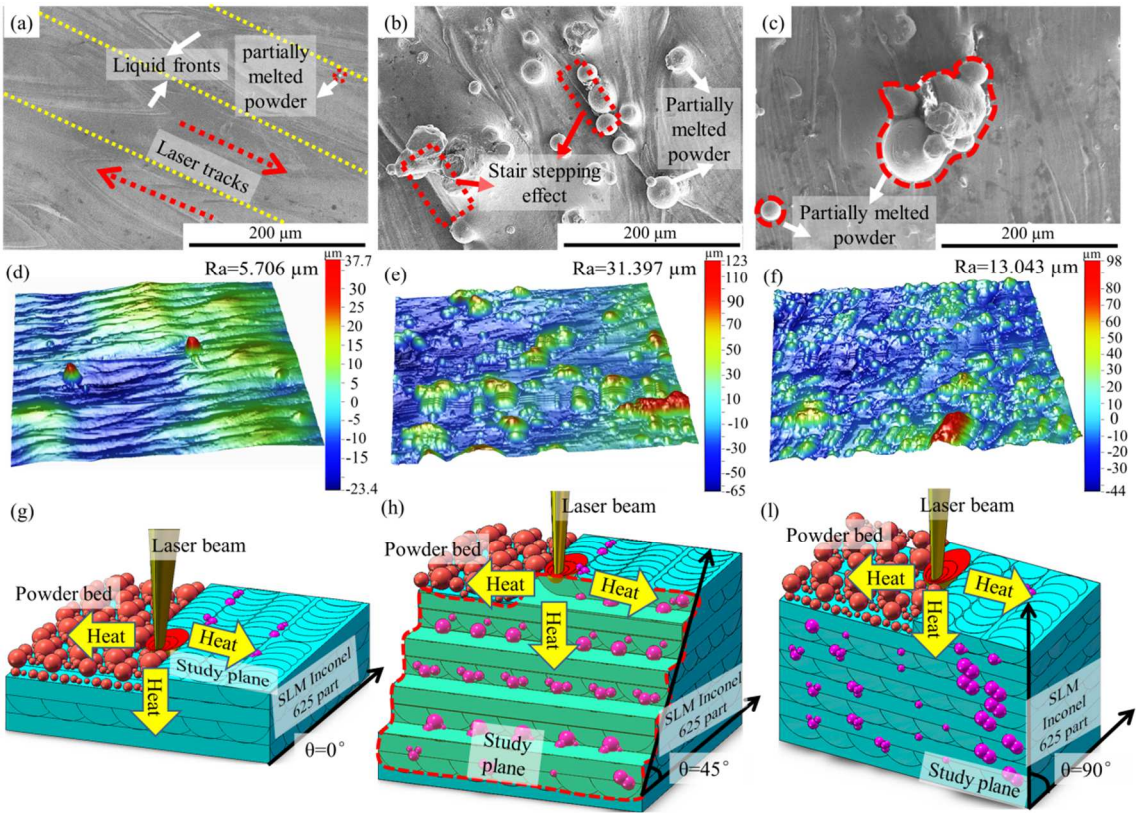

Figure 3. SEM macroscopic morphology of the SLM samples: (a) 0°; (b) 45°; (c) 90°; three-dimensional surface topographies of the SLM specimens: (d) 0°; (e) 45°; (f) 90°; surface roughness formation mechanism of the SLM parts: (g) 0°; (h) 45°; (l) 90°.

To investigate the impact of applying different building directions on the surface roughness, the surface morphology of the SLM Inconel 625 samples processed in different printing directions is shown in Fig. 3. The SLM 0° sample showed a relatively smooth surface having only a small number of partially melted powder particles within the borders between the neighboring tracks (Fig. 3a). Whereas, in the SLM 45° sample, plenty of partially melted particles were noticeable on the interfaces between the adjacent layers, which are thought to be essentially caused by the prominent stair steps (Fig. 3b). Similarly, multiple partially melted powder particles were found in the SLM 90° sample (Fig. 3c). However, it is noted that these small stair steps were no longer present in the SLM 90° sample compared to that in the SLM 45° sample. Moreover, the above macrostructure characteristics (Fig. 3a-c) were quantitatively analyzed by the Ra measurement of these samples (Fig. 3d-f). The SLM 0° sample had the smoothest surface (Ra=5.706 μm), while the SLM 45° sample exhibited the roughest surface (Ra=31.397 μm).

To further understand the influence of the building orientations on the surface roughness of the printed parts, the forming mechanism of the observed macroscopic morphology is presented in Fig. 3g-l. It is known that the balling phenomenon (Gu and Shen, 2009) and the stair stepping effect (Strano et al., 2013), also promoting the occurrence of the balling phenomenon, are the essential factors affecting the surface roughness of the SLM parts produced under the different building orientations. With regard to the balling phenomenon, the micro-sized balls and large-sized balls can be assumed as the two major types of balling phenomenon. When the preset powder bed is irradiated by the laser beam, the molten pool having heterogeneous surface tension is produced, owing to the different volumes of different elements existing in the molten pool based on the study of Steen and Mazumder (2010). The partial kinetic energy of the laser beam is converted into the surface energy of the molten metal, due to a high scanning velocity producing some smaller metal droplets of alloy material. To ensure that these droplets have a minimum surface energy, a variety of micro-sized balls will be formed under the joint influence of the surface tension and gravity. Besides, a small quantity of metal droplets also tend to splash from the surface of the molten pool and then solidify into the micro-sized balls on the surface of the SLM parts.

In general, the phenomenon of forming the micro-sized balls is uncommon due to the limited kinetic energy created by the high scanning velocity. The relatively smooth surface observed on the macro-surface appearance of the SLM 0° sample (Fig. 3a and Fig. 3g) is an evidence for this claim. Additionally, the laser remelting process existing in these overlapping regions is beneficial for inhibiting the balling phenomenon and improving the surface finish of SLM parts (Yasa and Kruth, 2011). Consequently, the smoothest macroscopic surface could be obtained on the SLM 0° sample.

Moreover, the formation of the large-sized balls on the macroscopic surface is rather typical, which can be marked as a wetting problem between the molten metal and the surface of the solidified SLM parts. The equilibrium of interfacial free energies existing among the

molten metal, the solidified printed samples and the ambient air can be governed by (Das, 2003):

$$S = \gamma_{sg} - \gamma_{sl} - \gamma_{lg}$$

where S is the spreading coefficient and γ_{sg}, γ_{sl} and γ_{lg} are the interfacial energies of the solid-gas, the solid-liquid and the liquid-gas, respectively. According to the above equation, the value of the S reflects the degree of spontaneous liquid spreading. The molten pool of the SLM Inconel 625 parts is inevitably susceptible to oxidation during the rapid solidification process, due to the existence of some active elements (e.g., Ni, Cr, etc.) prone to oxidation in the composition of these samples (Das, 2003). However, the γ_{sg} of these metal oxides are quite lower than the corresponding γ_{lg} (Bunnell et al., 1995) causing a negative S. Hence, under this condition, the molten metal tends to diminish surface energy by forming dozens of large-sized balls, instead of wetting the metal oxide films. Furthermore, owing to the extremely short dwelling time of the laser beam (normally less than 4 ms, as demonstrated by Simchi (2006) and Simchi and Pohl (2004)) and the exceedingly high solidification rate of the molten pool (up to 30 m/s, as reported by Gholipour et al. (2011) and Rack and Kalish, (1974)), the molten metal cannot perfectly wet the surface. This phenomenon, therefore, facilitates the formation of the large-sized balls on the surface of the printed samples.

As a result, the large-sized balls were detected on the macroscopic surfaces of the SLM 45° sample (Fig. 3b) and the SLM 90° sample (Fig. 3c). Moreover, the macro-surface appearance of the SLM 45° sample (i.e., the study plane shown in Fig. 3h) was composed of multiple micro-sized stair steps. Since there doesn't exit the remelting process in the regions of the stair steps, therefore, the balling effect produced on the surface of the previous cladding layer cannot be eliminated. Consequently, under the combined effect of the balling effect and stair stepping effect, the value of the surface roughness of the SLM 45° sample is the largest. As for the surface of the SLM 90° sample, it is noted that, thanks to the remelting phenomenon occurred between the neighboring layers, a relatively fine surface finish is obtained. However, the balling phenomenon especially the large-sized balls was also evident (Fig. 3c and Fig. 3l) in the sample prepared under this condition.

3.3.2 Microstructure evolution

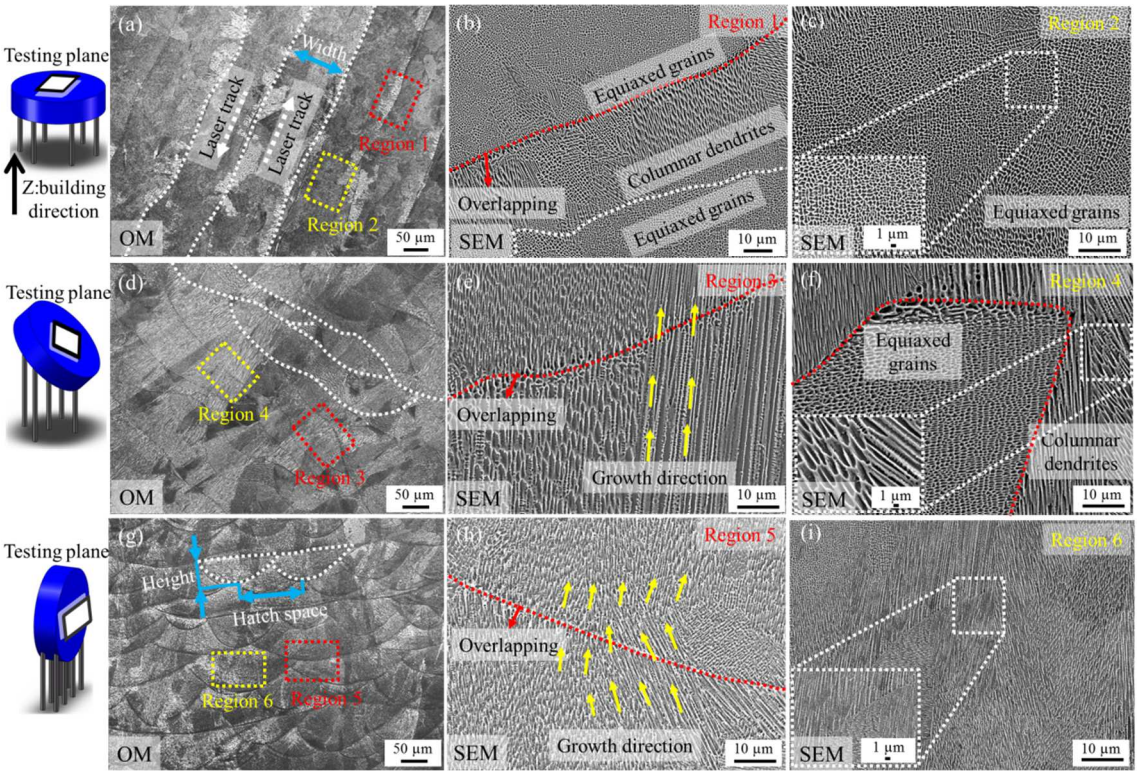

Figure 4. Microstructures of the SLM parts: (a) the SLM 0° sample; (b) enlarged view of region 1 in a; (c) enlarged view of region 2 in a; (d) the SLM 45° specimen; (e) enlarged view of region 3 in d; (f) enlarged view of region 4 in d; (g) the SLM 90° part; (h) enlarged view of region 5 in g; (i) enlarged view of region 2 in g.

Fig. 4 presents the microstructures of the SLM parts, manufactured in different building directions (0°, 45°, 90°) using OM and SEM. As for the microstructure of the SLM 0° sample, the width of the laser track shown in Fig. 4a was approximately 86-108 μm, which was basically equal to the laser spot size (100 μm). The microstructure close to the overlapping line (region 1) was mainly composed of columnar dendrites (near the overlapping line) and equiaxed grains (near the middle of the laser tracks), as depicted in Fig. 4b. In contrast, basically only fine equiaxed grains with a size of about 0.38-0.63 μm (region 2) existed in the middle of the laser tracks as displayed in Fig. 4c. Fig. 4d shows the large fish-scale shape molten pool distributed within the microstructure of the SLM 45° sample. The coarse columnar structures and equiaxed grains were still observed next to the overlapping line (region 3) between these two adjacent layers (Fig. 4e). Fig. 4f illustrates that the columnar structures were grown on the surfaces of the equiaxed grains with a size of approximately 0.73-1.26 μm (in the region 4). The fish-scale morphology with the size of 21-45 μm in height, formed in the SLM 90° specimen, was roughly equal to the powder layer thickness (30 μm). In addition, the distance between the neighboring tracks (about 105-129 μm), measured from the Fig. 4g, was substantially equivalent to the hatch space. As displayed in Fig. 4h and

Fig. 4i, the columnar dendrites and equiaxed grains (about 0.45-0.91 μm). Interestingly, both existed in the overlapping regions between the adjacent laser layers (region 5) and in the molten pool (region 6).

In short, after observing and analyzing the microstructures of the SLM parts in different building directions, it is found that the microstructures, regardless of the building orientations, are primarily made up of columnar dendrites and equiaxed grains.

It should be noted that in these specimens the finest microstructure and the largest number of equiaxed grains were distributed in the SLM 0° sample, while, the SLM 45° sample possessed the coarsest microstructure and the least quantity of equiaxed grains. In order to explain the above phenomenon, the influence of the building directions on the surface microstructure evolution process is analyzed. The microstructure features in Fig. 4 can be characterized and analyzed by considering the surface microstructure evolution process of multi-tracks (region A) and multi-layers (region B) of the SLM Inconel 625 parts, as depicted in Fig. 5. The heat input (Q_s) distribution in the molten pool can be estimated by the Gaussian heat source and thus the corresponding Q_s is expressed below (Luo et al., 2018):

$$Q_s = Q_m \exp(-\frac{2r^2}{R^2})$$

where Q_m is the maximum heat flux density; r is the radial distance between the observing point and the laser spot center and R is the laser spot radius. Therefore, in the same plane irradiated by the laser beam, as r gradually increases, the heat input amount will gradually decrease. This trend will result in the temperature in the middle of the molten pool to be much higher than that in the boundary region of the molten pool. In the central area of the molten pool, the convective heat transfer process occurs mainly in two directions, i.e., from the center to the periphery of the molten pool, and from the surface of the molten pool to the ambient environment. This phenomenon will make the actual temperature (T_q) gradient in the liquid metal at the central region of the molten pool much lower than the liquidus temperature (T_l) gradient. Consequently, the resulted large degree of constitutional undercooling ($\Delta T = T_L - T_q$) satisfies the nucleation conditions of the equiaxed grains. Hence, a heterogeneous crystal nucleation process in the central region of the molten pool will occur, and they will gradually grow into polyhedral grains, i.e., stage 1 (as shown in Fig. 5b).

Based upon the requirement for the minimum Gibbs free energy, crystal interfaces are often composed of crystal planes with lower interfacial energy. Therefore, the polyhedral surfaces formed are the interfaces with low interfacial energies, while, the “corner” regions are crystal planes with high interfacial energies. According to the XRD spectrums (as displayed in Fig. 2), it can be interpreted that the crystal plane of the minimum interfacial energy of the γ phase grains in the SLM Inconel 625 component is {111} crystal plane. In a non-equilibrium solidification process of the molten pool, a solute concentration gradient in the liquid metal at the front of the polyhedron is high and thus the diffusion speed is quite large. It is owing to this reason that the growth morphology of the polyhedral grains is shown

in stage 2. When the equiaxed grains rapidly grow larger and approach each other, the grain boundaries tend to have equal angles and the intersecting interface of three grains will be preferentially formed (remarked in stage 3). To meet a requirement of the minimum grain boundary energy, as displayed by Callister and Rethwisch. (2015) among these grains, the following equation can be presented:

$$\frac{\gamma_{1-2}}{\sin\alpha_3} = \frac{\gamma_{2-3}}{\sin\alpha_1} = \frac{\gamma_{3-1}}{\sin\alpha_2}$$

where $\gamma_{1\text{-}2}$, $\gamma_{2\text{-}3}$, and $\gamma_{3\text{-}1}$ are interfacial tensions; α_1, α_2, α_3 are interface angle between adjacent grains. Thus, in the final stage, the interface angles between adjacent grains will be prone to be 120° and also be substantially equal. Finally, the equiaxed grains at the center of the molten pool exhibit hexagonal structures (as shown in stage 4). Besides, since the marginal area of the molten pool is surrounded by the powder bed, the temperature gradient at the edge of the molten pool will be much greater than that at the center of the molten pool. Additionally, there is little difference in the solidification rate between the center area and the boundary area of the molten pool. Under such conditions, the columnar dendrites will form and distribute along the margin of the molten pool.

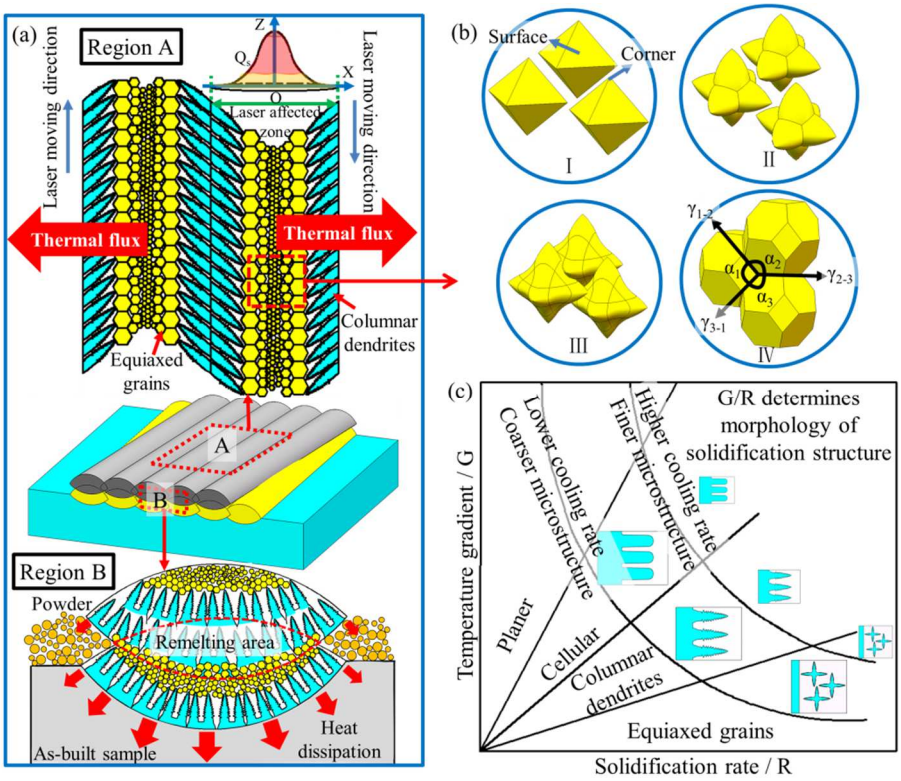

Figure 5. (a) Surface microstructure characteristics of the multi-tracks and the multi-layers regions of the SLM parts; (b) equiaxed grains formation mechanism diagram; (c) schematic profile illustrating the effects of temperature gradient G and growth rate R on the morphology of solidification microstructure described by Liu et al. (2016).

Combining the above analysis and Fig. 5c, the microstructure of the SLM 0° sample is the one with the multi-tracks overlapping region (as depicted in region A of Fig. 5a). The

microstructure evolution from the boundary of the laser track to the middle of that consist of separately coarse columnar dendrites, fine columnar dendrites, coarse equiaxed grains and fine equiaxed grains. This microstructure features denote that the columnar dendrites primarily grew along the laser tracks (as shown in Fig. 4b), while, the equiaxed grains were distributed in the center of that (as displayed in Fig. 4c).

Regarding the SLM 45° specimen, its microstructure is substantially equivalent to the microstructure of the SLM 90° sample being intercepted at a 45° angle. The microstructure of the SLM 90° sample is the one with the multi-layers region (as illustrated in region B of Fig. 5a). Hence, the microstructure formation mechanism of both samples can be depicted by region B of Fig. 5a and the microstructure evolution of these two specimens can be principally determined using the heat dissipation direction, the preferred orientation of the dendrites, and the ratio of the temperature gradient (G) to the solidification rate (R) (Fig. 5c). At the bottom of the molten pool, since G, close to the substrate, is rather small and R is quite large, therefore, a typical characteristic of epitaxial columnar growth perpendicular to the interface of the molten pool will occur. In the middle of the molten pool, due to the further reduction of G/R, fine dendritic structures are distributed on the surface of the coarse columnar dendrites. Moreover, since the heat dissipation direction of the solidification microstructure is mainly through the multi-layers region and powder bed, the growth orientation of the dendrites is only in the opposite direction of the heat dissipation direction. This results in the directional growth of the columnar structures (as shown in Fig. 4e and Fig. 4h). Ascending from the middle of the molten pool, the G is the lowest and the R is the largest, so the value of G/R is the smallest. Consequently, in addition to the formation of the fine dendrites, the fine equiaxed grains can be also formed at the top of the molten pool (as demonstrated in Fig. 4f and Fig. 4i.). As for the remelting areas, the microstructure will maintain the growth direction of the microstructure in the previous layers and continue to grow because of the phenomenon of structural inheritance. This feature not only ensures the bonding strength between the adjacent layers but also makes the epitaxial structure have continuity in the growth direction (Fig. 4e). Another interesting phenomenon in the remelting zone is that the melt flow will produce a scouring effect on the solute-rich layer at the front of the columnar dendrites. This makes the columnar dendrites grow obliquely just like Fig. 4h.

3.3 Microhardness

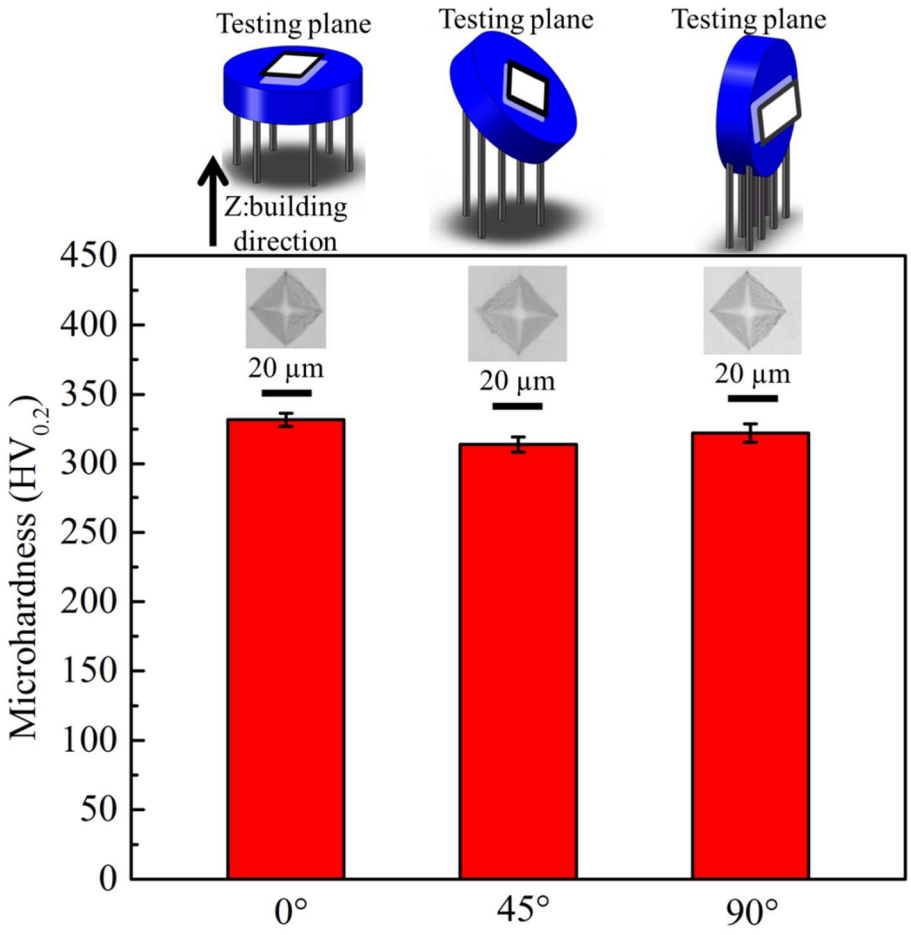

Figure 6. Microhardness of the SLM parts built in different building directions

As presented in Fig. 6, the average microhardness of the SLM 0° sample, the SLM 45° sample and the SLM 90° sample is 332 $HV_{0.2}$, 314 $HV_{0.2}$ and 322 $HV_{0.2}$, respectively. The mechanical performances of the SLM samples have a strong correlation to their microstructure characteristics. Comparing these three types of the SLM samples built in different orientations, the massive fine equiaxed grains distributed within the surface microstructure of the SLM 0° sample have a significant effect on the improvement of its hardness. In contrast, the comparably coarse columnar dendrites and equiaxed grains formed in the surface of the SLM 45° and the SLM 90° samples will induce lower hardness values in these samples as compared to the SLM 0° one. Additionally, the average microhardness of the SLM 45° part is the lowest among these specimens by the cause of having the coarsest microstructure.

3.4 Anisotropy in tribological properties

3.5.1 Coefficient of friction and wear rate

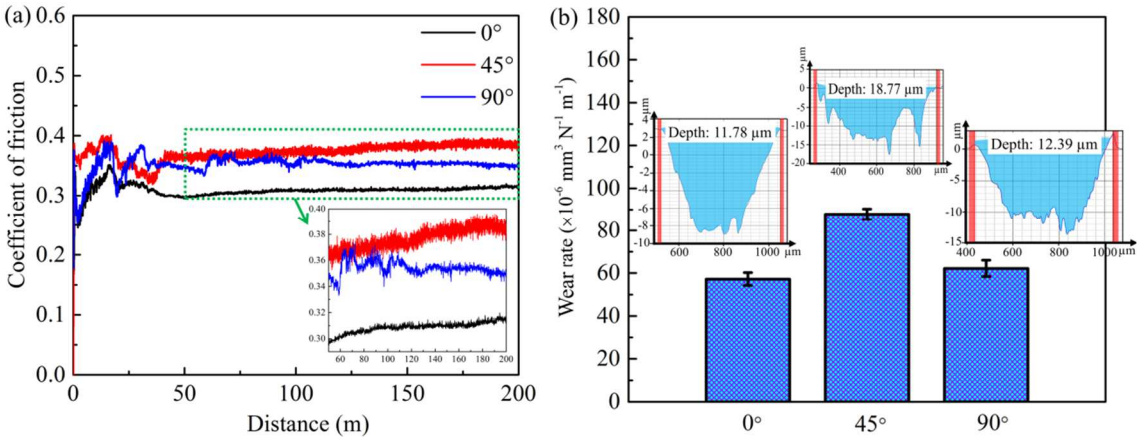

Figure 7. (a) COF - distance profiles and (b) wear rate of the SLM samples fabricated in the different building directions.

Fig. 7 displays the effect of the building directions on the tribological properties including the COF and wear rate of the SLM specimens. The corresponding statistical results are listed in Table 3. As for the SLM 0° sample, the average COF of the stable stage of friction (i.e., the wear distance from 50 m to 200 m) is 0.31 and the average wear rate is only 57.2×10^{-6} mm^3/(N•m). In contrast, the average COF and the wear rate of the SLM 45° sample and the SLM 90° sample are relatively higher, as compared to the SLM 0° one. These can be attributed to the coarser columnar dendrites and equiaxed grains dispersed within the surface of these specimens as compared to the SLM 0° one. As a result, amongst these parts, the SLM 45° sample exhibits the worst tribological performance, as it contains the coarsest surface microstructure.

Table 3: Tribological properties of SLM Inconel 625 specimens produced in different building orientations

Sample	Average COF	Average wear rate ($\times10^{-6}$ mm^3 /(N•m))
SLM 0° part	0.31	57.2±3
SLM 45° part	0.38	87.8±2.5
SLM 90° part	0.35	62.2±3.8

3.5.2 Worn track morphology and mechanism

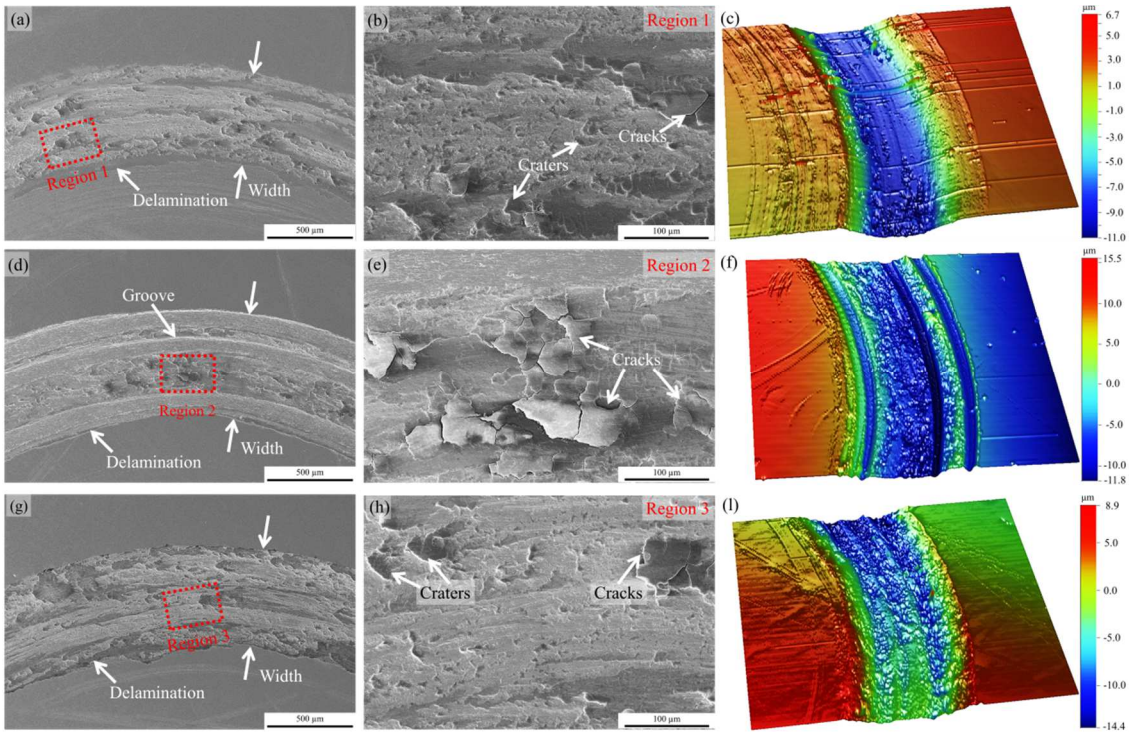

Figure 8. Worn surface morphology of (a) SLM 0° sample; (b) magnified view of region 1 in a; (c) 3D surface topography of a; (d) SLM 45° sample; (e) magnified view of region 2 in d; (f) 3D surface topography of d; (g) SLM 90° sample; (h) magnified view of region 3 in g; (l) 3D surface topography of g.

Details about the worn surface morphology of the SLM Inconel 625 parts are revealed in Fig. 8. For the SLM 0° specimen, the average width of the worn track was about 531.6 μm. Numerous grooves and furrows were scattered on the surface of the worn track, illustrating that the main wear mechanism causing damage during the test was abrasive. A small quantity of micro craters and cracks could also be presented in region 1 (Fig. 8b), which demonstrate the occurrence of delamination in the worn surface. The 3D surface topography of the SLM 0° sample after experiencing the friction stage was relatively smooth (Fig. 8c). While, as for the SLM 45° part, the width of the worn track was 646.5 μm (Fig. 8d). As depicted in Fig. 8d-e, a great number of cracks and parallel deep grooves were presented on the worn surface of this sample which is indicative of delamination and deformation phenomenon occurring on the worn surface. Thus, the 3D surface topography of the SLM 45° part was comparably rougher than that of the SLM 0° part (Fig. 8f). As seen in Fig. 8g, the width of the wear track for the SLM 90° sample was 602.6 μm. In addition, a small number of cracks and craters were produced due to the plowing effect. This indicated that the ploughing were also another primary wear mechanism damaging this sample. It is noted that the 3D surface of the wear trace of the SLM 90° sample was rather smoother than that of the SLM 45° part.

In short, the abrasive and micro-ploughing wear mechanisms are the main wear

mechanism damaging these SLM Inconel 625 parts. Moreover, it is concluded that the effect of the building directions on the tribological performances of these samples (such as average COF, wear rate and worn track morphology) cannot be neglected. Hence, the influence of the printing orientations upon the wear performance and the friction behavior of the samples are discussed below.

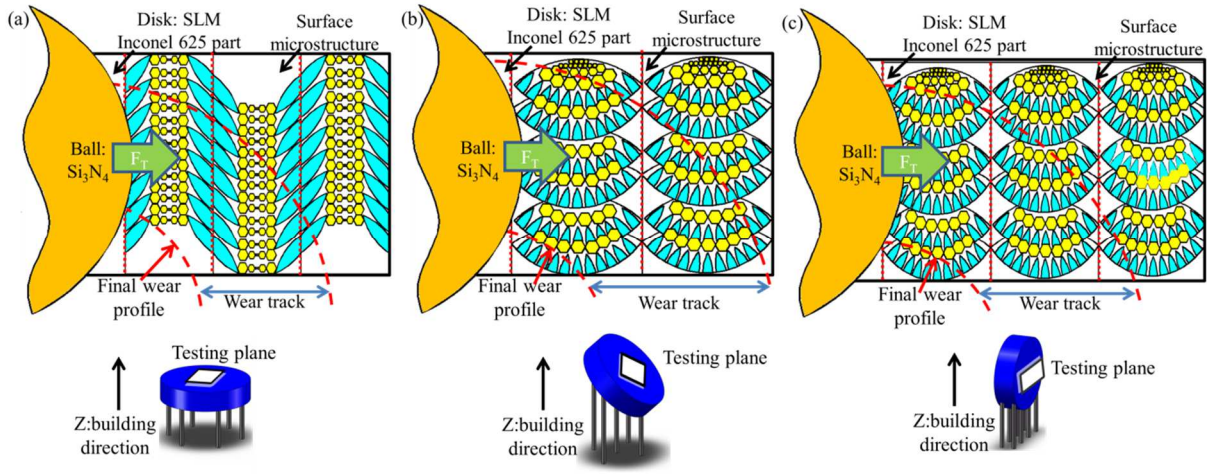

Figure 9. Schematic diagrams of sliding wear mechanism on the surface of the SLM Inconel 625 parts manufactured at different printing directions: (a) 0°; (b) 45°; (c) 90°.

Fig. 9 illuminates the relationship between the surface microstructure and the wear mechanism of the SLM Inconel 625 samples manufactured in different building orientations. Compared with the columnar dendrites, the fine equiaxed grains are easier to accommodate large strains announced by Martin et al. (2017). During the sliding wear process, thus, the columnar dendrites are liable to break up under the tangential force (F_T) resulting in a poor wear resistance performance.

Among these specimens, the finest microstructure (e.g., columnar dendrites and equiaxed grains) were primarily formed in the surface of the SLM 0° specimen (Fig. 4a-c). Therefore, under the illustration of Fig. 9a, as the columnar structures are peeled off during the wear process, the equiaxed grains will be also gradually peeled off. Then, upon the influence of this process, some inconspicuous plows (Fig. 8a), a small quantity of micro craters, and some micro cracks (Fig. 8b) were progressively formed on the worn track surface. As mentioned, this phenomenon produced the smoothest worn surface with the narrowest average width of the worn track (Fig. 8c) in SLM 0° sample. On the contrary, according to the surface microstructure analysis of the SLM 45° specimen (Fig. 4d-f), the roughest columnar dendrites and the smallest number of equiaxed grains were dispersed within the microstructure of the SLM 45° component. Consequently, according to Fig. 9b, after a large quantity of rough columnar dendrites are peeled off in the process of the sliding wear, a huge number of craters and cracks are produced in the damaged areas. As the wear process is further performed, these numerous micro craters and cracks will connect to each other, and then produce the massive larger cracks. This phenomenon could be observed in Fig. 8e.

Hence, the roughest worn trace surface with the largest average width of the worn track was obtained in this sample, as displayed in Fig. 8f. As for the SLM 90° component, under the description of Fig. 4g-l, the surface microstructure of the SLM 90° sample was finer than that of the SLM 45° part and the proportion of the equiaxed grains in the microstructure was more than that of the SLM 45° specimen. Therefore, under the illumination of Fig. 9c, only a small quantity of columnar structures within the surface of the SLM 90° specimen will begin to break up and generate some tiny craters and cracks during the dry sliding wear process. As compared to the SLM 45° part, these craters and cracks were not joined together but only scattered on the worn surface of the SLM 90° specimen (Fig. 8g-h). Finally, as seen in Fig. 8l, a relatively rough worn surface was obtained.

4 Conclusion

In summary, a variety of SLM Inconel 625 samples were successfully fabricated by SLM technology to study the effect of the building directions upon the performances of the SLM parts. In this work, experiments were conducted to investigate the impact of the building orientations on the surface roughness, microstructure evolutions, and tribological properties of the selective laser melted Inconel 625 parts. Primary conclusions drawn from this work were listed as follows:

1. The phase structure of the SLM Inconel 625 specimens was predominately composed of the γ-Ni (fcc) phase. The lattice constant of the γ-Ni phase in the SLM 45° sample (3.59204 Å) was lowest than other SLM samples. The microstructure of the SLM parts was composed of the columnar structures and the equiaxed grains. Among these samples, the finest microstructure and the largest number of equiaxed grains (0.38-0.63 μm) were distributed in the SLM 0° sample, while, the SLM 45° sample possessed the coarsest microstructure and the least quantity of equiaxed grains (0.73-1.26 μm).
2. The value of the surface roughness of the SLM 45° sample (31.397 μm) was the roughest owing to the balling phenomenon and the stair stepping effect. On the contrary, the value of the surface finish of the SLM 0° specimen (5.706 μm) was the smoothest due to the remelting phenomenon.
3. For the SLM 0° specimen, the average COF and the wear rate was 0.31 and 57.2×10^{-6} mm^3 / (N•m), respectively. In contrast, for the SLM 45° sample, the average COF and the wear rate was respectively 0.38 and 87.8×10^{-6} mm^3 /(N•m).

The present work demonstrates that the SLM building direction has an obvious influence on the surface macro- / micro- structure and tribological properties of the Inconel 625 parts. This paper will attract the attention of the engineering community for designing a proper building direction to obtain a desirable surface with better tribological performances.

Acknowledgement

The author reports no conflicts of interests in this work. As one of the authors, Xingchen Yan, is grateful for the financial supports provided by Special Fund Project of GDAS (2021GDASYL-20210102005), Sciences Platform Environment and Capacity Building Projects of GDAS (2019GDASYL-0402006, 2019GDASYL-0402004, 2019GDASYL-0502006, 2018GDASCX-0402, 2018GDASCX-0111 and 2019GDASYL-0501009), Guangzhou Project of Science & Technology (201909010008, 201807010030), Guangdong province Science and Technology Plan Projects (2017A070701027, 2017A070702016, 2014B070705007 and 2017B030314122). The author, Cheng Chang would like to thank the support from the program of CSC (201801810106). The author, Shuohong Gao would like to thank the support from the program of CSC (201801810066).

References

Alexander, L., Klue, H.P., 1989. Basic aspects of x-ray absorption in quantitative diffraction analysis of powder mixtures. Powder Diffr. 4, 66–69. https://doi.org/10.1017/S0885715600016432

Aliofkhazraei, M., 2015. Superalloys. BoD–Books on Demand.

Anam, A., Dilip, J.J.S., Pal, D., Stucker, B., 2014. Effect of Scan Pattern on the Microstructural Evolution of Inconel 625 during Selective Laser Melting. Int. Solid Free. Fabr. Symp. – An Addit. Manuf. Conf. 363–376. https://doi.org/10.13140/2.1.1256.6089

Bunnell, D., Das, S., Bourell, D., Beaman, J., Marcus, H., 1995. Fundamentals of liquid phase sintering during selective laser sintering. Int. Solid Free. Fabr. Symp. 3, 440–447.

Callister, W.D., Rethwisch., D.G., 2015. Materials science and engineering: an introduction, 9th ed. New York: John wiley & sons.

Chen, C., Xie, Y., Yan, X., Yin, S., Fukanuma, H., Huang, R., Zhao, R., Wang, J., Ren, Z., Liu, M., Liao, H., 2019. Effect of hot isostatic pressing (HIP) on microstructure and mechanical properties of Ti6Al4V alloy fabricated by cold spray additive manufacturing. Addit. Manuf. 27, 595–605. https://doi.org/10.1016/j.addma.2019.03.028

Cieslak, M.J., Headley, T.J., Kollie, T., Romig, A.D., 1988. Melting and solidification study of Alloy 625. Metall. Trans. A, Phys. Metall. Mater. Sci. 19 A, 2319–2331. https://doi.org/10.1007/BF02645056

Das, S., 2003. Physical Aspects of Process Control in Selective Laser Sintering of Metals. Adv. Eng. Mater. 5, 701–711. https://doi.org/10.1002/adem.200310099

Dinda, G.P., Dasgupta, A.K., Mazumder, J., 2009. Laser aided direct metal deposition of Inconel 625 superalloy: Microstructural evolution and thermal stability. Mater. Sci. Eng. A 509, 98–104. https://doi.org/10.1016/j.msea.2009.01.009

Frazier, W.E., 2014. Metal additive manufacturing: A review. J. Mater. Eng. Perform. 23, 1917–1928. https://doi.org/10.1007/s11665-014-0958-z

Gholipour, A., Shamanian, M., Ashrafizadeh, F., 2011. Microstructure and wear behavior of stellite 6 cladding on 17-4 PH stainless steel. J. Alloys Compd. 509, 4905–4909. https://doi.org/10.1016/j.jallcom.2010.09.216

562 Gonzalez, J.A., Mireles, J., Stafford, S.W., Perez, M.A., Terrazas, C.A., Wicker, R.B., 2019. Characterization of
563 Inconel 625 fabricated using powder-bed-based additive manufacturing technologies. J. Mater. Process.
564 Technol. 264, 200–210. https://doi.org/10.1016/j.jmatprotec.2018.08.031
565 Graulis, S., Chateigner, D., Downs, R.T., Yokochi, A.F.T., Quirós, M., Lutterotti, L., Manakova, E., Butkus, J.,
566 Moeck, P., Le Bail, A., 2009. Crystallography Open Database - An open-access collection of crystal
567 structures. J. Appl. Crystallogr. 42, 726–729. https://doi.org/10.1107/S0021889809016690
568 Gu, D., Shen, Y., 2009. Balling phenomena in direct laser sintering of stainless steel powder: Metallurgical
569 mechanisms and control methods. Mater. Des. 30, 2903–2910. https://doi.org/10.1016/j.matdes.2009.01.013
570 Li, C., White, R., Fang, X.Y., Weaver, M., Guo, Y.B., 2017. Microstructure evolution characteristics of Inconel
571 625 alloy from selective laser melting to heat treatment. Mater. Sci. Eng. A 705, 20–31.
572 https://doi.org/10.1016/j.msea.2017.08.058
573 Li, S., Wei, Q., Shi, Y., Chua, C.K., Zhu, Z., Zhang, D., 2015. Microstructure Characteristics of Inconel 625
574 Superalloy Manufactured by Selective Laser Melting. J. Mater. Sci. Technol. 31, 946–952.
575 https://doi.org/10.1016/j.jmst.2014.09.020
576 Liu, S., Li, Y., Liu, F., Zhang, H., Ding, H., 2016. Effects of relative positioning of energy sources on weld
577 integrity for hybrid laser arc welding. Opt. Lasers Eng. 81, 87–96.
578 https://doi.org/10.1016/j.optlaseng.2016.01.010
579 Luo, C., Qiu, J., Yan, Y., Yang, J., Uher, C., Tang, X., 2018. Finite element analysis of temperature and stress
580 fields during the selective laser melting process of thermoelectric SnTe. J. Mater. Process. Technol. 261,
581 74–85. https://doi.org/10.1016/j.jmatprotec.2018.06.001
582 Martin, J.H., Yahata, B.D., Hundley, J.M., Mayer, J.A., Schaedler, T.A., Pollock, T.M., 2017. 3D printing of
583 high-strength aluminium alloys. Nature 549, 365–369. https://doi.org/10.1038/nature23894
584 Materials Information Company, 1991. ASM International Handbook Committee, Properties and selection: irons
585 steels and high performance alloys. ASM Handb. 1872–1873.
586 https://doi.org/10.31399/asm.hb.v01.a0001046
587 Mumtaz, K., Hopkinson, N., 2009. Top surface and side roughness of Inconel 625 parts processed using selective
588 laser melting. Rapid Prototyp. J. 15, 96–103. https://doi.org/10.1108/13552540910943397
589 Paul, C.P., Ganesh, P., Mishra, S.K., Bhargava, P., Negi, J., Nath, A.K., 2007. Investigating laser rapid
590 manufacturing for Inconel-625 components. Opt. Laser Technol. 39, 800–805.
591 https://doi.org/10.1016/j.optlastec.2006.01.008
592 Rack, H.J., Kalish, D., 1974. STRENGTH, FRACTURE TOUGHNESS, AND LOW CYCLE FATIGUE
593 BEHAVIOR OF 17-4 PH STAINLESS STEEL. Met. Trans 5, 1595–1605.
594 https://doi.org/10.1007/BF02646331
595 Rashid, R., Masood, S.H., Ruan, D., Palanisamy, S., Rahman Rashid, R.A., Elambasseril, J., Brandt, M., 2018.
596 Effect of energy per layer on the anisotropy of selective laser melted AlSi12 aluminium alloy. Addit. Manuf.
597 22, 426–439. https://doi.org/10.1016/j.addma.2018.05.040
598 Simchi, A., 2006. Direct laser sintering of metal powders: Mechanism, kinetics and microstructural features. Mater.
599 Sci. Eng. A 428, 148–158. https://doi.org/10.1016/j.msea.2006.04.117
600 Simchi, A., Pohl, H., 2004. Direct laser sintering of iron-graphite powder mixture. Mater. Sci. Eng. A 383, 191–
601 200. https://doi.org/10.1016/j.msea.2004.05.070
602 Song, K.H., Nakata, K., 2010. Effect of precipitation on post-heat-treated Inconel 625 alloy after friction stir
603 welding. Mater. Des. 31, 2942–2947. https://doi.org/10.1016/j.matdes.2009.12.020
604 Steen, W.M., Mazumder, J., 2010. Laser Material Processing, Vasa. Springer Science & Business Media.
605 Strano, G., Hao, L., Everson, R.M., Evans, K.E., 2013. Surface roughness analysis, modelling and prediction in

606 selective laser melting. J. Mater. Process. Technol. 213, 589–597.
607 https://doi.org/10.1016/j.jmatprotec.2012.11.011
608 Uriondo, A., Esperon-Miguez, M., Perinpanayagam, S., 2015. The present and future of additive manufacturing in
609 the aerospace sector: A review of important aspects. Proc. Inst. Mech. Eng. Part G J. Aerosp. Eng. 229,
610 2132–2147. https://doi.org/10.1177/0954410014568797
611 Yadollahi, A., Shamsaei, N., 2017. Additive manufacturing of fatigue resistant materials: Challenges and
612 opportunities. Int. J. Fatigue 98, 14–31. https://doi.org/10.1016/j.ijfatigue.2017.01.001
613 Yadroitsev, I., Pavlov, M., Bertrand, P., Smurov, I., 2009. Mechanical properties of samples fabricated by
614 selective laser melting. 14èmes Assises Eur. du Prototypage Fabr. Rapide 625, 24–25.
615 Yadroitsev, I., Smurov, I., 2010. Selective laser melting technology: From the single laser melted track stability to
616 3D parts of complex shape. Phys. Procedia 5, 551–560. https://doi.org/10.1016/j.phpro.2010.08.083
617 Yan, X., Chang, C., Dong, D., Gao, S., Wenyou, M.A., Liu, M., Liao, H., Yin, S., 2020a. Microstructure and
618 mechanical properties of pure copper manufactured by selective laser melting. Mater. Sci. Eng. A 139615.
619 https://doi.org/10.1016/j.msea.2020.139615
620 Yan, X., Chen, C., Chang, C., Dong, D., Zhao, R., Jenkins, R., Wang, J., Ren, Z., Liu, M., Liao, H., Lupoi, R.,
621 2020b. Study of the microstructure and mechanical performance of C-X stainless steel processed by
622 selective laser melting (SLM). Mater. Sci. Eng. A 781, 139227.
623 https://doi.org/10.1016/j.msea.2020.139227
624 Yan, X., Li, Q., Yin, S., Chen, Z., Jenkins, R., Chen, C., Wang, J., Ma, W., Bolot, R., Lupoi, R., Ren, Z., Liao, H.,
625 Liu, M., 2019a. Mechanical and in vitro study of an isotropic Ti6Al4V lattice structure fabricated using
626 selective laser melting. J. Alloys Compd. 782, 209–223. https://doi.org/10.1016/j.jallcom.2018.12.220
627 Yan, X., Yin, S., Chen, C., Jenkins, R., Lupoi, R., Bolot, R., Ma, W., Kuang, M., Liao, H., Lu, J., Liu, M., 2019b.
628 Fatigue strength improvement of selective laser melted Ti6Al4V using ultrasonic surface mechanical
629 attrition. Mater. Res. Lett. 7, 327–333. https://doi.org/10.1080/21663831.2019.1609110
630 Yap, C.Y., Chua, C.K., Dong, Z.L., Liu, Z.H., Zhang, D.Q., Loh, L.E., Sing, S.L., 2015. Review of selective laser
631 melting: Materials and applications. Appl. Phys. Rev. 2. https://doi.org/10.1063/1.4935926
632 Yasa, E., Kruth, J., 2011. Application of Laser Re-Melting on Selective Laser Melting Parts. Adv. Prod. Eng.
633 Manag. 6, 259–270.
634 Yen, Y. wen, Su, J. wei, Huang, D. ping, 2008. Phase equilibria of the Fe-Cr-Ni ternary systems and interfacial
635 reactions in Fe-Cr alloys with Ni substrate. J. Alloys Compd. 457, 270–278.
636 https://doi.org/10.1016/j.jallcom.2007.03.053
637

Surface roughness formation mechanism

(a)
Z:building direction
Testing plane
Powder bed
Laser beam
Heat
Heat
Heat
Study plane
SLM Inconel 625 part
θ=0°

(b)
Laser beam
Powder bed
Z:building direction
Testing plane
Heat
Heat
Heat
Study plane
θ=45°

(c)
Laser beam
Powder bed
Z:building direction
Testing plane
Heat
Heat
Heat
SLM Inconel 625 part
Study plane
θ=90°

Microstructure characteristics

(a)
Region A
Z
Q_s
X
O
Laser affected zone
Laser moving direction
Laser moving direction
Thermal flux
Thermal flux
Columnar dendrites
Equiaxed grains
A
B
Region B
Powder
Remelting area
As-built sample
Heat dissipation

Schematic diagrams of sliding wear mechanism

(a)
Disk: SLM Inconel 625 part
Surface microstructure
Ball: Si_3N_4
F_T
Final wear profile
Wear track

(b)
Disk: SLM Inconel 625 part
Surface microstructure
Ball: Si_3N_4
F_T
Final wear profile
Wear track

(c)
Disk: SLM Inconel 625 part
Surface microstructure
Ball: Si_3N_4
F_T
Final wear profile
Wear track